

Performance of the MICE diagnostic systems

5

The MICE Collaboration

Abstract

Muon beams of low emittance provide the basis for the intense, well-characterised neutrino beams of a neutrino factory and for multi-TeV lepton-antilepton collisions at a muon collider. The international Muon Ionization Cooling Experiment (MICE) has demonstrated the principle of ionization cooling, the technique by which it is proposed to reduce the phase-space volume occupied by the muon beam at such facilities. This paper documents the performance of the detectors used in the MICE experiment to measure the muon-beam parameters. The integration of the instrumentation in a comprehensive diagnostic system will also be described.

1 Introduction

Either a muon collider or a neutrino factory would require having high intensity and the phase-space volume occupied by the muon beam to be reduced before the injection into the storage ring [1]. Due to the lifetime of the muon, the only feasible cooling technique would be the ionisation cooling [2] where muons pass through material before being re-accelerated. The net effect would be a reduction of the transverse emittance while the longitudinal energy is restored. MICE, demonstrating for the first time this technique [3], has made the idea of those facility a concrete possibility for the future.

MICE was operated parasitically of the ISIS proton synchrotron, based at the Rutherford Appleton Laboratory (STFC). ISIS accelerates protons up to 800 MeV at a repetition rate of 50 Hz, while a titanium target is dipped nearly once per second in the outer halo of the proton beam. Pions are generated in the interaction and captured inside the MICE beamline by a set of quadrupoles and dipoles (figure 1). Pions inside the Decay Solenoid decay to muons. The transported beam initial emittance is altered before entering in the cooling channel by a set of adjustable diffusers providing further multiple scattering.

MICE was instrumented with a range of detectors used for particle identification and position-momentum measurement as described in this paper, used to fully characterise the beam and its evolution across the cooling channel.

30 2 Time-of-Flight Detectors

2.1 Introduction

Three time-of-flight detectors (TOF0, TOF1, TOF2) were built and installed at RAL in 2008 and 2009 to measure the position and the time of crossing particles. TOF0 and TOF1 [4][5][6] were placed upstream of the cooling channel, and TOF2 [7] was downstream of the channel, mounted in front of the KL, as shown in figure 1. The time of flight between two TOF stations provides particle identification information and can also be used for momentum measurement. TOF1 served most of the time also as an experimental trigger. They operated smoothly during the running periods of the MICE experiment and were essential for all the measurements done [8][9].

The good performances of the TOF detectors, over an extended period of time, enabled the MICE experiment to characterise fully its muon beams during the early stages of data-taking, by measuring their emittance [10] and assessing their pion contamination [11].

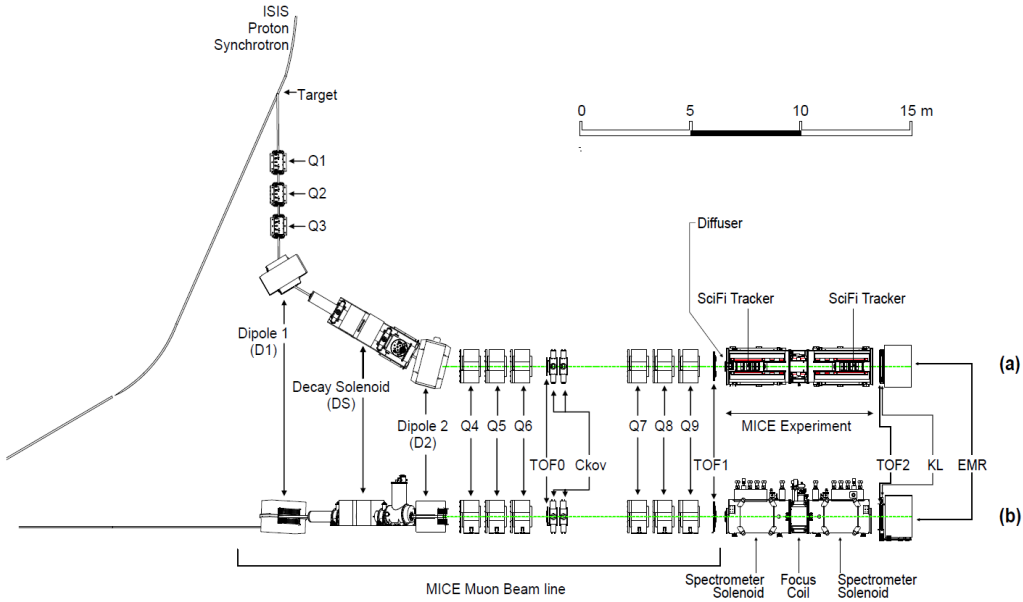


Figure 1: MICE experiment, showing the full beam line starting from the target position on the proton synchrotron) with the full set of quadrupoles and dipoles (Q1 to Q9, D1/2), the Decay Solenoid, and cooling channel elements with all the detectors.

Each TOF station was made of two planes of 1" scintillator bars oriented along X and Y directions, respectively. The bars were made of BC404 plastic scintillator. A simple fishtail light-guide was used to attach each end of each bar to R4998 Hamamatsu fast photomultiplier tubes. R4998 PMTs were delivered by Hamamatsu in assemblies (H6533MOD) that included the PMT tube, the voltage divider chain and a 1 mm thick μ -metal shield, extending 30 mm beyond the photocathode surface. To increase the count-rate stability, active dividers were used. Illustration of a TOF detector is shown in figure 2 together with an exploded view of a slab.

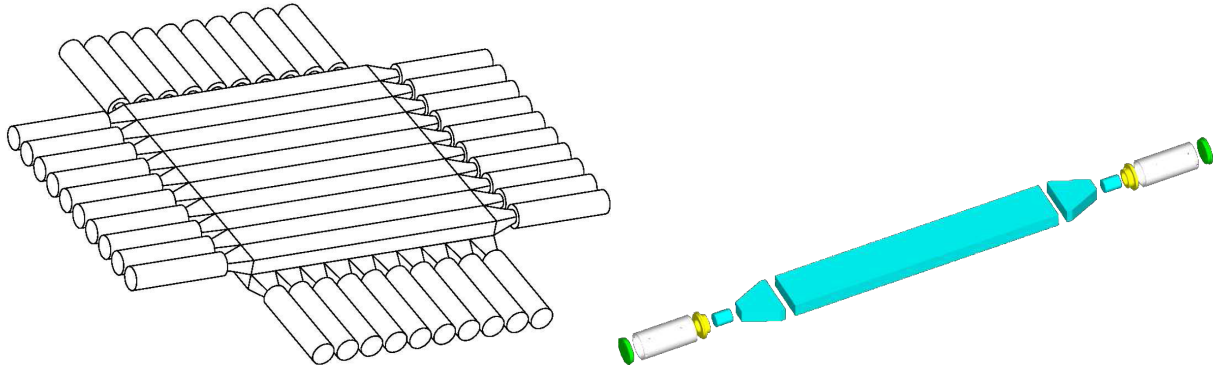


Figure 2: Design of the TOF detector structure showing the horizontal and vertical layers of slabs (left) and details of each slab showing one scintillator with on each side the light-guides and the PMTs (right) [4].

The stations TOF0, TOF1, and TOF2 had active areas of $40 \times 40 \text{ cm}^2$, $42 \times 42 \text{ cm}^2$, and $60 \times 60 \text{ cm}^2$ respectively. Each of the planes in TOF0 had 10, 4 cm wide, scintillator slabs. Stations TOF1 and TOF2 were composed by 7 and 10 scintillator slabs in each plane, respectively. The PMTs were connected to a 50% – 50% passive splitter using RG213 signal cable. One half of the signal was fed to the leading-edge CAMAC Lecroy 4115 discriminator followed by CAEN V1290 TDC for time measurement. The second half of the signal went to CAEN V1724 FADC for pulse-height measurement. Pulse height measurement is essential for time-walk

corrections. Each electronic issued a local readout trigger if signals in both PMTs attached to a slab crossed a specific threshold. All three stations were read out when TOF1 station issued a local trigger. This readout trigger was also used for the rest of the MICE detector systems.

All stations were exposed to residual magnetic fields: TOF0 was placed in a relatively low residual field produced by the last quadrupole magnet of the beam line (which had mirror plates installed), while the other two TOF stations were exposed to the stray fields of the cooling channel solenoids. A shielding structure was adopted covering all PMTs at each side of the stations [6].

The purpose of the TOF system was to discriminate particle species based on time-of-flight measurement. The main components in the MICE beam are muons, pions, and positrons. The time resolution needed to be sufficiently good to effectively discriminate between these types. At $240\text{ MeV}/c$, the time-of-flight difference between muon and pion was about 1.3 ns between TOF0 and TOF1 stations. With 200 ps resolution, one reached near 100% discrimination efficiency [12].

2.1.1 Calibration Method

Measurement of time traversal of a particle through a TOF station is influenced by several factors at the hardware level. When a particle crosses the plastic scintillator, there is a short delay in light production, with a characteristic decay time of 1.8 ns.

After generation, scintillation light propagates to the ends of each scintillator slab where it is detected by photomultiplier tubes. The light-travel time depends on the distance of the particle crossing from the PMT. The lengths of slabs in TOF0, TOF1, and TOF2 were 40 cm, 40 cm, and 60 cm, respectively. This translates to about 3.0 ns, 3.1 ns, and 4.4 ns of light travel time, respectively, as the effective light propagation speed in the scintillator was found to be approximately 13.5 cm/ns. More delay was introduced by the transit time of each PMT and of the cable that led the signal to the readout electronics. These times were unique for each individual PMT channel and needed to be determined in dedicated measurements.

A simple linear discriminator measured the time of each signal coming from a PMT. This introduced bias in the measured time dependent on the total charge of the signal, an effect referred to as time-walk.

Signal times of each channel were recorded in TDC boards. Readout of the whole system was triggered by having a signal in TOF1. The readout trigger signal is distributed to all TDC boards and is used as a reference time. Which PMT channel's threshold crossing caused the readout was dependent on where the particle crossed through the TOF1 station. As a consequence, the reference time had a bias dependent on the position of the TOF1 crossing, an effect referred to here as trigger delay. To compensate this, the final time measurement in each station was determined as an average of the times of individual channels.

Corrections which need to be made to the measured times are then the time-walk correction, the PMT channel specific delay time and a correction for the reference trigger time delay [13].

2.1.2 Reconstruction

A particle crossing a TOF station must have crossed 2 orthogonal slabs in the station's 2 planes. The time and approximate position of a particle crossing a TOF station was reconstructed from the PMT signals in the two slabs. Each slab with at least one recorded signal in each of the 2 PMTs was considered as being crossed by a particle. Times of these recorded signals were corrected for time-walk, readout trigger signal delay, and the channel specific delay. Time of crossing of the slab was then taken as the average of the 2 corrected PMT times.

The 2 slabs hit by a particle defined a pixel of area given by the width of the slabs. Sometimes, there were more slabs in each plane with signals. Matching of 2 slabs being crossed by a particle was done based on their

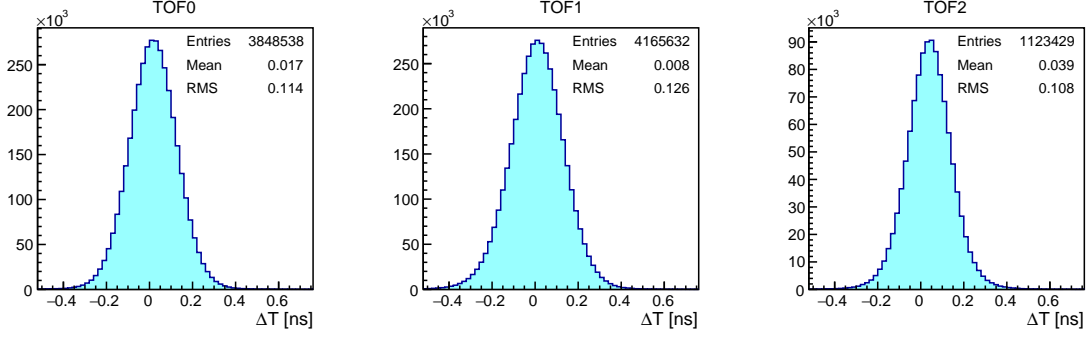


Figure 3: Overall slab ΔT distributions. Total width of the distribution is due to the resolution of individual pixels and due to the offsets in their ΔT distributions.

95 measured signal time. They were matched if the times were within a 4 ns window. The time of the particle crossing was determined as the average of times of the 2 matched slabs.

2.2 Performance

Resolution of time-of-flight measurement is given by time resolution of each station. The time associated to each TOF is determined from the average of the times when the two slabs (horizontal and vertical) are crossed 100 by a particle. The resolution of the average is a half of the spread of their difference. Therefore, looking at slab ΔT allows the time-of-flight resolution to be determined.

Overall performance can be inferred from the combined slab ΔT distributions. The plots in figure 3 show that they all centre approximately at 0 ns and they exhibit very similar resolutions, with TOF1 having the largest spread. Figure 4 shows an example of measurement of time of flight between the first two stations, 105 TOF0 and TOF1. Times of electrons, muons, and pions are clearly separated, creating peaks from left to right, respectively. The observed width of the electron peak of approximately 0.11 ns is about 30% larger than the calculated spread from a naive addition of slab ΔT of the individual TOF stations. This difference is attributed to contributions to the resolution of individual stations which cancel out in the slab ΔT measurement, and to variations in the travelled path length of the electrons between stations TOF0 and TOF1.

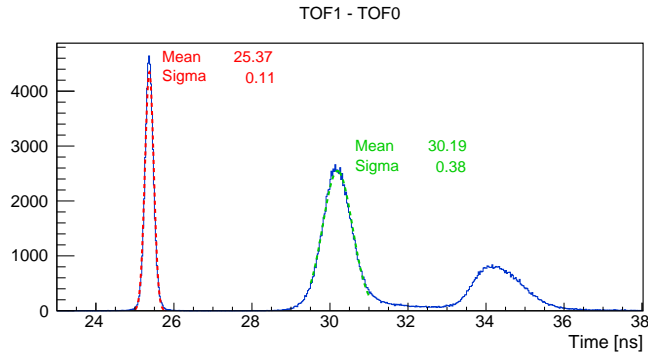


Figure 4: Time of flight between TOF0 and TOF1 for a “pion” beam after all corrections have been applied. From the left: the well separated electron, muon and pion peaks.

¹¹⁰ **3 Cherenkov Detectors**

3.1 Introduction

The MICE threshold Cherenkov detectors, measuring velocity, are primarily designed to provide π - μ separation in the higher momentum ranges, where TOF separation of the two species peaks is not sufficient for conclusive particle identification.

¹¹⁵ In order to provide separation over a large range of momenta, two high-density silica aerogel Cherenkov detectors (CkovA and CkovB) with refractive indices $n=1.07$ and $n=1.12$ are used. Light is collected in each counter by four 9354KB eight-inch UV-enhanced PMTs and recorded by CAEN V1731 FADCs (500 MS/s). The two detectors are placed directly one after another in the beamline, located just after the first TOF counter. In figure 5 an exploded view of one detector is shown.

¹²⁰ Their respective thresholds provide different responses in four distinct momentum ranges, i.e. in the 200 MeV/c beams, pions are below the threshold which would fire the detector for both CkovA and CkovB whereas muons are above the threshold only for CkovB, while for the 240 MeV/c beams, pions are above the threshold for CkovB while muons are above for both CkovA and CkovB. This can be used to distinguish particle species. Below the CkovB muon threshold of about 217.9 MeV/c, where there is no separation, the TOFs provide good ¹²⁵ separation, whereas the momentum range above the CkovA pion threshold 367.9 MeV/c was outside of the MICE running parameters [14]. For unambiguous identification of particle species the Cherenkov detectors would need a momentum measurement from the MICE tracker.

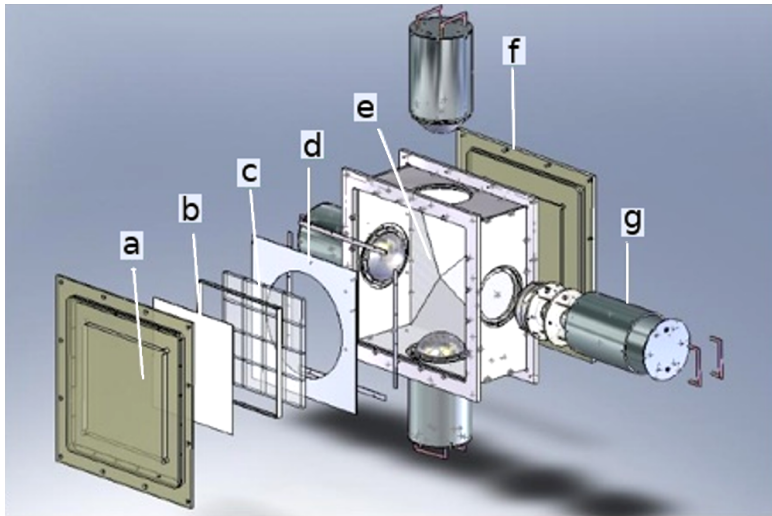


Figure 5: MICE aerogel Cherenkov counter blowup: a) entrance window, b) mirror, c) aerogel mosaic, d) acetate window, e) GORE reflector panel, f) exit window and g) eight-inch PMT in iron shield.

3.2 Performance

A wide range beam momenta (including alignment runs) has been used in order to cover the full spectra of ¹³⁰ particles that could have been measured by the Cherenkov detectors. The asymptotic light yield (for $\beta=v/c=1$) in each counter were measured using the electron peaks, giving 16 ± 1 photoelectrons (NPE) in CkovA and 19 ± 1 in CkovB.

The photoelectrons yields versus momentum for muons and pions in CkovA and CkovB are displayed in figure 6, using the time of flight between TOF0 and TOF1 to select the species and to estimate the momentum.
135 The distributions $N(P)$ of NPEs as a function of the momentum P were fitted with the function

$$N(P) = N_0 + N_{\beta=1} \left(1 - \left(\frac{P_0}{P} \right)^2 \right) \quad (1)$$

where N_0 is the number of background photoelectrons, $N_{\beta=1}$ is the asymptotic light yield and P_0 is the momentum threshold.

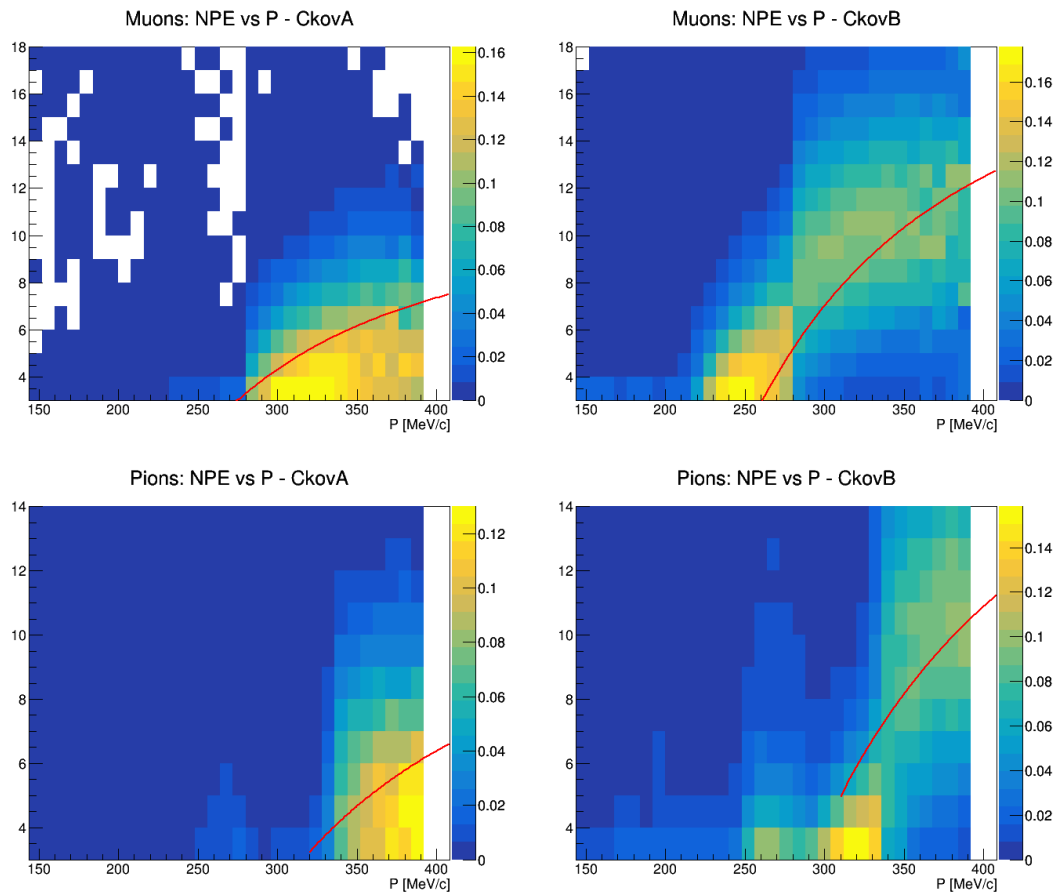


Figure 6: Photoelectron yields versus momentum for muons and pions in CkovA and CkovB with the superimposed fitted activation functions.

The observed muon thresholds are 267.3 ± 18.1 and 219.4 ± 14.5 MeV/c, while for pions are 332.2 ± 38.4 MeV/c and 295.9 ± 95.9 MeV/c, respectively in CkovA and CkovB. The $NPE_{\beta=1}$ values are generally
140 lower than the values predicted as in a previous analysis [14]: this is mostly due to TOF0 acting as a pre-shower radiator.

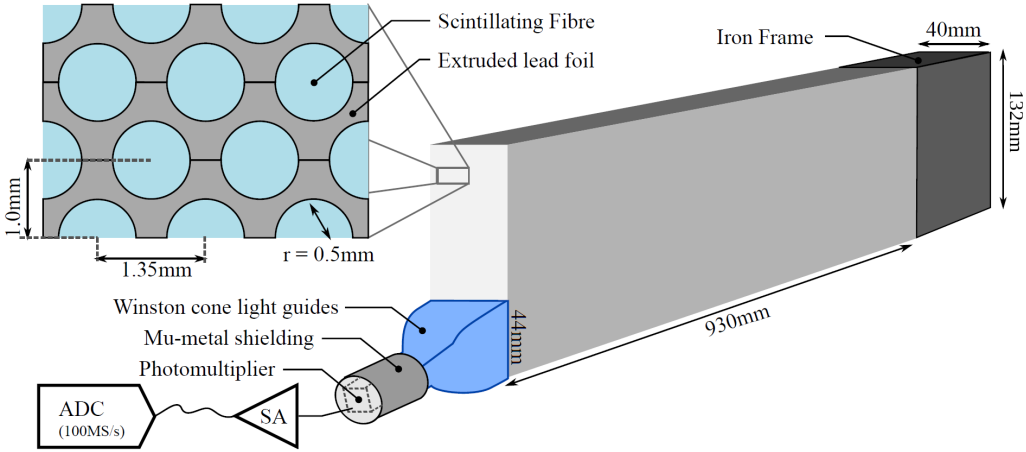


Figure 7: Single slab design of MICE KLOE-Light Calorimeter.

4 KLOE-Light Calorimeter

4.1 Introduction

The KLOE-Light (KL) pre-shower sampling calorimeter is composed of extruded lead foils in which scintillating fibres are placed in. The volume ratio of scintillator and lead is approximately 2 to 1, “lighter” than the one of the KLOE experiment calorimeter (1 to 1).

The fibres are 1 mm diameter BICRON BCF-12, scintillating in the blue, 1.35 mm distant from each other within a layer. The distance between two layers is 0.98 mm, one layer being shifted by half the fibre pitch with respect to the next. Scintillation light is guided from each slab into a total of six PMTs (three on each side). Iron shields are fitted to each photomultiplier to mitigate against large stray magnetic fields from the cooling channel. The signal from each PMT is sent to a shaping amplifier (SA) module, which shapes and stretches the signal in time in order to match the sampling rate of the flash ADCs (figure 7 shows the design of a single slab). A total of 7 slabs forms the whole detector, which has an active volume of $93\text{ cm} \times 93\text{ cm} \times 4\text{ cm}$.

With its 2.5 radiation lengths the KL is used to distinguish muons from decay electrons providing energy deposition and timing information and to act as pre-shower in front of the EMR. The detector has been used to estimate the level of pion contamination within the MICE muon beams to be around 1% [11].

4.2 Performance

The study of the KL response to different particle types (muons, pions and electrons) at different momenta is based on particle identification obtained by time-of-flight detector, as shown in the example of figure 4, by applying time cuts on the time-of-flight spectrum across the peaks of the different species. The performance is presented for beamline settings with nominal 140, 170, 200, 240 and 300 MeV/c momenta. The results presented below are obtained from the straight tracks runs (i.e. without magnetic fields in the trackers or focus coil). The KL response to muons, pions and electrons for all available momenta is presented in figure 8. It is clear in the cases of muons and pions that they are below mip momenta since energy deposition decreases with momentum increasing. Actually the energy deposition is defined as the sum of ADC products from all cells in KL above a given threshold. The ADC product on the other hand is the product of left and right side of one slab divided by the sum of left and right side: $\text{ADC}_{\text{prod}} = 2 \times \text{ADC}_{\text{left}} \times \text{ADC}_{\text{right}} / (\text{ADC}_{\text{left}} + \text{ADC}_{\text{right}})$. The factor 2 is present for normalisation. The product of two sides compensates the effect of attenuation.

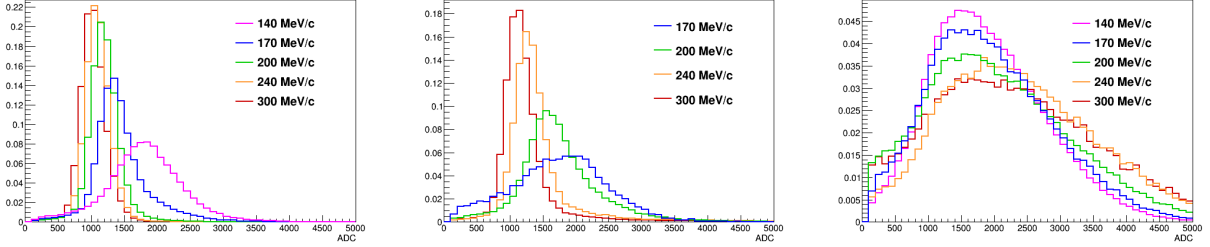


Figure 8: KL response to muons (left), pions (centre) and electrons (right) for all available momenta. The charge deposited by particles in KL in arbitrary units is shown. All histograms are normalised to unity.

For comparison of energy deposition of muon, pions and electrons for a fixed momentum is presented in
 170 figure 9. For example 300 MeV/c (figure 9, bottom) muons and pions have almost the same distribution, while moving to lower energies pions have a broader distribution, experiencing hadronic interactions and loosing more energy. This pion behaviour has been used to estimate its contamination in muon samples [11].

Species	140 MeV/c	170 MeV/c	200 MeV/c	240 MeV/c	300 MeV/c
electrons	0.95 ± 0.02	0.95 ± 0.01	0.94 ± 0.03	0.96 ± 0.02	0.95 ± 0.02
muons	0.97 ± 0.02	0.99 ± 0.01	0.99 ± 0.01	0.99 ± 0.01	0.99 ± 0.01
pions	n/a	0.89 ± 0.03	0.95 ± 0.03	0.97 ± 0.03	0.98 ± 0.01

Table 1: Efficiency of KL for electrons, muons and pions as a function of particle momentum. The conditions required are existing of a TOF track and signal in KL above the threshold. The uncertainties are statistical.

In figure 10 is shown simulation of KL response to 300 MeV/c muons and pions and the distributions are compared with data. The simulation takes into account the distribution of the photon in scintillator fibres, the
 175 subsequent creation of photoelectrons on photomultiplier photocathodes and the response of the photomultipliers (which gain is around 2×10^6). The agreement between data and simulation is very good.

5 Electron Muon Ranger

5.1 Introduction

The Electron-Muon Ranger (EMR) is a fully-active scintillator detector [15]. It can be classified as a tracking-calorimeter as its granularity allows for track reconstruction. The EMR consists of extruded triangular scintillator bars arranged in planes. One plane contains 59 bars and covers an area of 1.27 m^2 . Each even bar is rotated by 180° with respect to the odd one. A cross-section of bars and their arrangement in a plane is shown in figure 11. This configuration does not leave dead areas in the detector for particles crossing a plane with angles that do not exceed 45° with respect to the beam axis. Each plane is rotated through 90° with respect to
 180 the previous one, such that hits in a pair of neighbour planes define a horizontal and vertical (x, y) interaction coordinate. The light, produced when a particle crosses a bar, is collected by a wave-length shifting (WLS) fibre glued inside the bar. At both ends, the WLS fibre is coupled to clear fibres that transport the light to a PMT. Signals produced in a plane are read out collectively on one end by a single-anode PMT (SAPMT) for an integrated charge measurement and separately on the other by multi-anode PMTs (MAPMT) for individual bar hit reconstruction. The full detector is composed of 24 X-Y modules for a total active volume of
 185 190

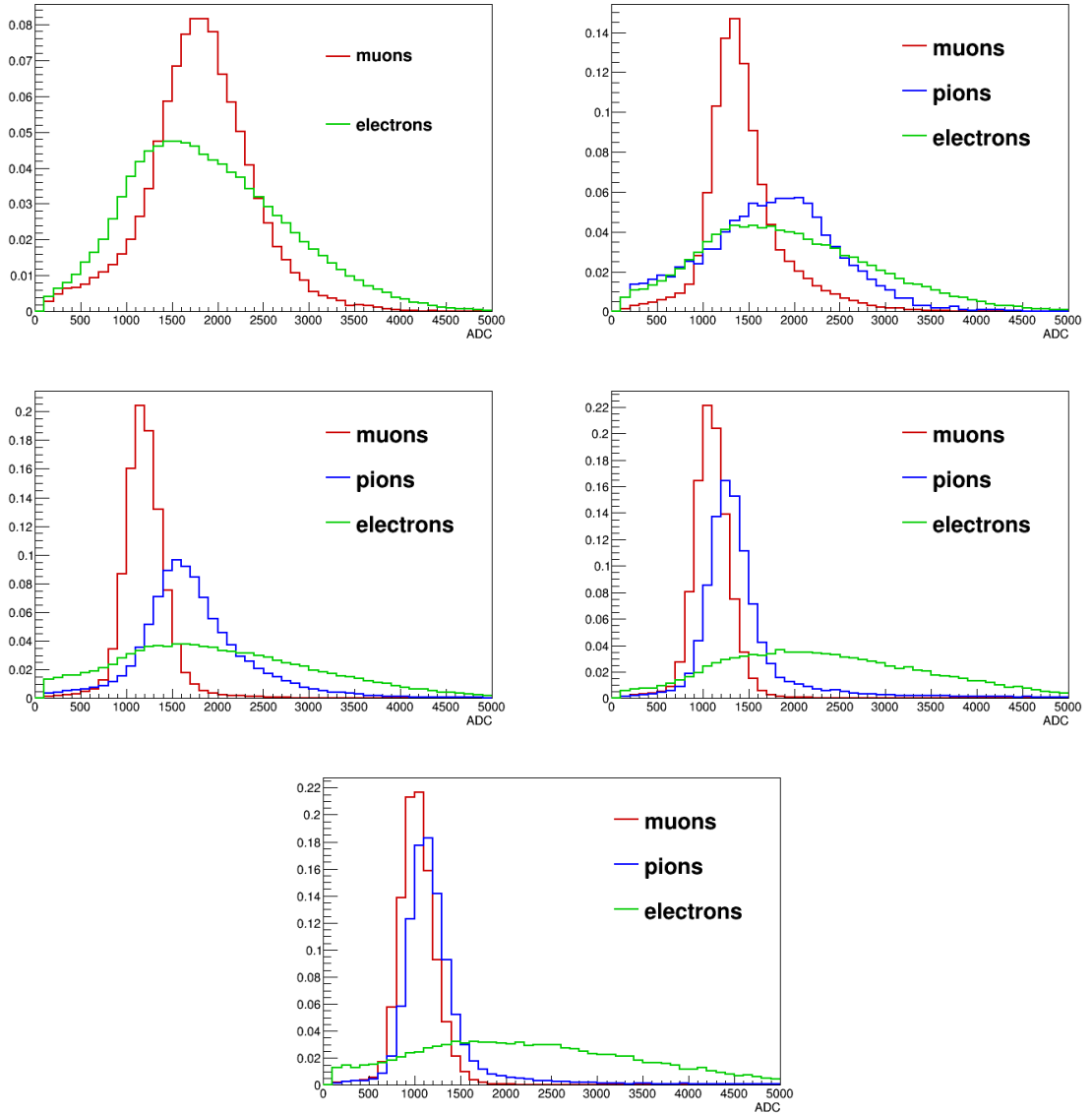


Figure 9: Comparison of energy deposition of muons, pions and electrons at 140 MeV/ c (top left), 170 MeV/ c (top right), 200 MeV/ c (middle left), 240 MeV/ c (middle right) and 300 MeV/ c (bottom).

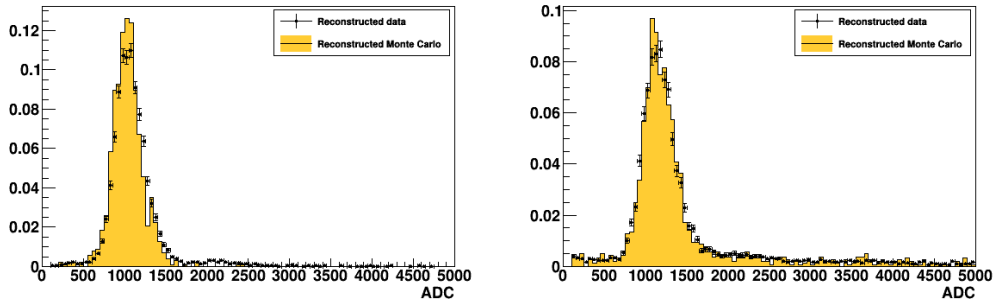


Figure 10: Comparison between data and Monte Carlo simulation of KL response to muons (left) and pions (right) at 300 MeV/ c .

approximately 1 m³.

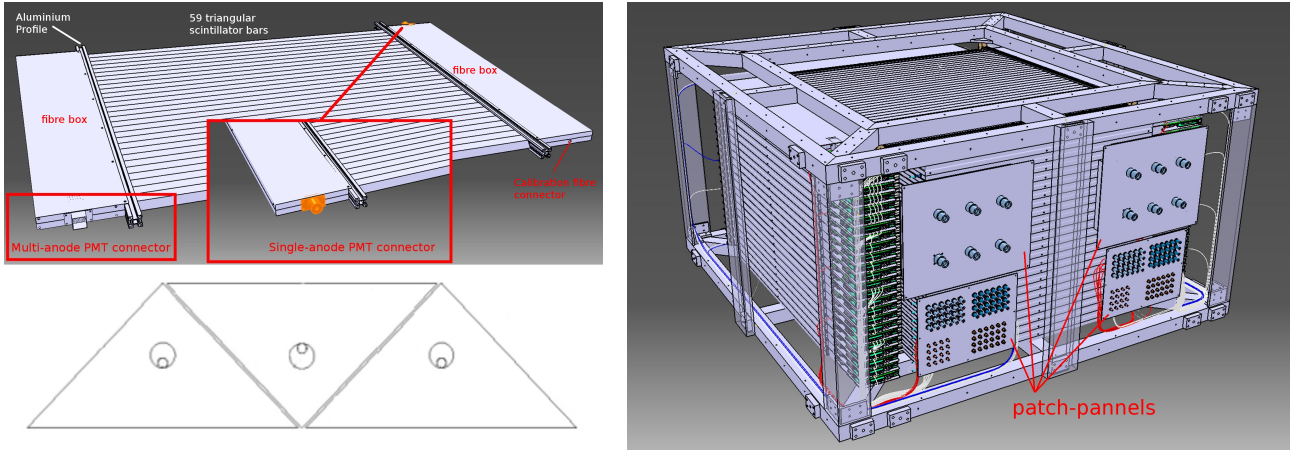


Figure 11: Drawing of one EMR plane (top left), cross section of 3 bars and their wavelength shifting fibres (bottom left) and drawing of the full detector and its supporting structure (right).

An array of analyses were conducted to characterise the hardware of the EMR and determine whether the detector performs to specifications [16]. The clear fibres coming from the bars were shown to transmit the desired amount of light, and only four dead channels were identified. The level of crosstalk is within acceptable values for the type of multi-anode photomultiplier used with an average of $0.20 \pm 0.03\%$ probability of occurrence in adjacent channels and a mean amplitude equivalent to $4.5 \pm 0.1\%$ of the primary signal intensity. The efficiency of the signal acquisition, defined as the probability of recording a signal in a plane when a particle goes through it in beam conditions, was $99.73 \pm 0.02\%$ [15].

The primary purpose of the EMR is to distinguish between muons and their decay products, identifying muons that have crossed the entire cooling channel. Muons and electrons exhibit distinct behaviours in the detector. A muon follows a single straight track before either stopping or exiting the scintillating volume. Electrons shower in the lead of the KL and create a broad cascade of secondary particles. Two main geometric variables, the plane density and the shower spread, are used to differentiate them. The detector is capable of identifying electrons with an efficiency of 98.6 %, providing a purity for the MICE beam that exceeds 99.8 %. The EMR also proved to be a powerful tool for the reconstruction of muon momenta in the range 100–280 MeV/c [17].

5.2 Performance

The performance of the EMR detector was assessed at three levels of resolution with data acquired during different period of data taking. The performance of the hardware itself was evaluated by analysing the characteristics of raw photomultiplier signals. The reconstruction efficiency was assessed. The performance of the detector as an electron tagging device was measured.

5.2.1 Hardware efficiencies

The MICE beam line was tuned to the highest attainable momentum to maximise the transmission to the EMR detector and increase the range of particles in the detector (approximately 400 MeV/c). In this configuration the beam line produces pions and muons in comparable quantities, along with positrons. The particle species are

identified by evaluating their time-of-flight between TOF1 and TOF2. Only the particles with a time-of-flight between 28 and 28.75 ns, i.e. compatible with the muon hypothesis, are included in the analysis sample.

A muon that makes it into the analysis sample has a momentum larger than 350 MeV/c right before TOF2. It is expected to cross both TOF2 and the KL without stopping and penetrate the EMR. In practice, the probability of creating an EMR event, i.e. to produce hits in the detector is $99.62 \pm 0.03\%$. The minor inefficiency may be attributed to pions in the muon sample that experience hadronic interactions in the KL. If hits are produced in the detector, space points are reconstructed $98.56 \pm 0.06\%$ of the times. The inefficiency may be associated with muons that decay between TOF2 and the EMR and produce scarce hits in the detector.

To evaluate the efficiency of the scintillator planes and their readouts, only the muons which penetrate the entire detector are used. If a signal is recorded in the most downstream plane, it is expected that at least a bar will be hit in each plane on its path and that a signal will be recorded in the single anode PMT. In $3.26 \pm 0.02\%$ of cases, on average, a plane traversed by a muon will be not produce a signal in its MAPMT and that the most probable amount of bars hit is one, while a track is missed by an SAPMT $1.88 \pm 0.01\%$ of the time.

5.2.2 Electron rejection

The main purpose of the EMR is to tag and reject the muons that have decayed in flight inside the experimental apparatus. A broad range of beam line momentum settings is used to characterise the muon selection efficiency. The particle species are characterised upstream of the detector by using the time-of-flight between TOF1 and TOF2 as shown before. The limits of the peaks are fitted to each setting in order to separate the muons and positrons into two templates upstream of the EMR. Particles that fall above the upper limit of the muon peak are either pions or slow muons and are rejected from this analysis.

MICE is a single-particle experiment, i.e. the signals associated with a trigger originate from a single particle traversing the detector. The multi-anode readout of each detector plane provides an estimate of the position of the particle track in the xz or the yz projection, depending on the orientation of the scintillator bars. Inside the detector the muon exhibits a clean straight track while the positron showers inside the lead of the KL and produces a disjointed and spread-out signature. Two particle identification variables based on these distinct characteristics can be defined. One is the plane density, ρ_p , defined as

$$\rho_p = \frac{N_p}{Z_p + 1}, \quad (2)$$

where N_p is the number of planes hit and Z_p the number of the most downstream plane. A muon deposits energy in every plane it crosses until it stops, producing a plane density close to one. A positron shower contains photons that may produce hits deep inside the fiducial volume without leaving a trace on their path, reducing the plane density. The second variable is the normalised chi squared, $\hat{\chi}^2$, of the fitted straight track, i.e.

$$\hat{\chi}^2 = \frac{1}{N - 4} \sum_{i=1}^N \frac{\text{res}_{q,i}^2 + \text{res}_{y,i}^2}{\sigma_x^2 + \sigma_y^2}, \quad (3)$$

where N is the number of space points (one per bar hit), $\text{res}_{q,i}$ the residual of the space point with respect to the track in the qz projection and σ_q the uncertainty on the space point in the qz projection, $q = x, y$ [18]. The number of degrees of freedom is $N - 4$, as a three-dimensional straight track has four parameters. This quantity represents the transverse spread of the particle's signature. A muon follows a single track and is expected to have a $\hat{\chi}^2$ close to one, while an electron shower is expected to produce a larger value. The two discriminating variables can be combined to form a statistical test on the particle hypothesis. Dense and narrow events will be tagged as muons while non-continuous and wide electron showers will not. The quality of a test statistic may

be characterised in terms of the loss, α , the fraction the muon sample that is rejected, and the contamination, β , the fraction of the electron sample that is selected.

The downstream tracker (TKD) allows for the reconstruction of particle momentum before entering the EMR. To assess the influence of momentum on contamination and loss, their values are calculated, because of the resolution, for 10 MeV/c bins in the range 100–300 MeV/c. The test statistic are calculated in each bin is based on the optimal set of cuts optimised for the whole sample, i.e. $\rho^* = 86.131\%$ and $\chi^{2*} = 14.229$. Figure 12 shows the loss, α , and the contamination, β , as a function of the momentum measured in TKD. It shows that, at low momentum, the apparent muon loss increases. This is due to an increase in decay probability between TOF2 and the EMR and an decrease in the number of muons that cross the KL to reach the EMR.

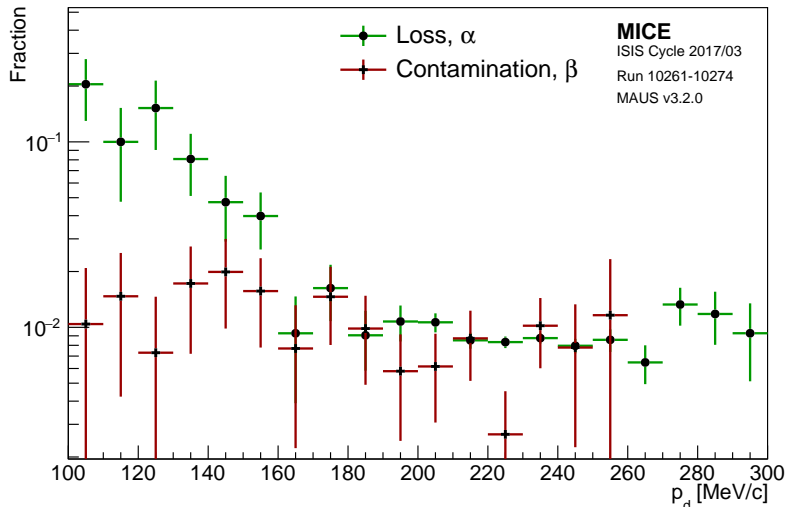


Figure 12: Percentage of electron contamination, β , and muon loss, α , for different ranges of momentum measured in the downstream tracker, p_d . The error bars are based on the statistical uncertainty in a bin.

6 Trackers

6.1 Introduction

MICE is equipped with two identical, high precision scintillating-fibre trackers, described in [19]. One tracker, TKU, is upstream of the cooling cell, the other, TKD, is downstream, the mirror image of TKU as shown in figure 1. Each tracker is placed in a superconducting solenoid (SSU and SSD, upstream and downstream respectively) designed to provide a uniform magnetic field over the tracking volume.

The trackers are 110 cm in length and 30 cm in diameter (see figure 13). There are five stations per tracker (labelled 1 to 5, with station 1 being closest to the cooling cell) held in position using a carbon-fibre space-frame. The stations sit at different distances in z (beam axis) of 20–35 cm: this ensures that the azimuthal rotation of track position from one station to the next differs, difference being important in the resolving ambiguities at the pattern-recognition stage. Each tracker is instrumented with an internal LED calibration system and four 3-axis Hall probes to monitor the field.

The tracker stations consists of three doublet layers of 350 μm scintillating fibres, these layers are arranged such that each is at an angle of 120° with respect to the next. This arrangement ensures that there are no inactive regions between adjacent fibres. Bundles of seven fibres are grouped into a single readout channel (this reduces



Figure 13: Photograph of one of the MICE Trackers, showing the five stations and the three doublet planes of scintillating fibres, each plane at 120° angles to the next (the central fibres of plane can be seen as darker lines traversing the station). Bundles of seven $350\ \mu\text{m}$ fibres are grouped together, to be read out by 1 mm scintillating fibre light guides.

the number of readout channels, while maintaining position resolution). The trackers have a spatial resolution per doublet layer of $470\ \mu\text{m}$ and an expected light yield of approximately 10 photo-electrons.

The light from the seven scintillating fibres passes into a single clear fibre, which takes it to a visible light photon counter (VLPC) which operate at 9 k. The signals from the VLPCs are digitised using electronics developed by the D0 collaboration [20].

6.2 Performance and Reconstruction

Each of the 15 tracker planes (three per station and five stations) consist of 214 channels, labelled 0–213, likewise each plane is assigned an integer plane number 0–2. Particle signals are recorded by the tracker electronics and calibrated channel by channel then converted into signal NPE. This information is then used to form a digit and is the first step in tracker reconstruction. Digit profiles are useful in identifying and rectifying or removing hot or dead channels in the planes and ensuring the accuracy of calibration. Smooth centrally peaked spectra are expected in a plane with no dead channels and minimal electronics noise, but this is not an essential requirement since it is the combination of two or three planes which go to make a point in the track and so there is redundancy built in. Hence a significant proportion of individual channels can be lost without a knock on drop in efficiency. The clustering algorithm loops over every combination of pairs of digits in a single event and combines any that occur in neighbouring channels. In the case of a multi-digit cluster, the unweighted average channel value is used to define the plane coordinate and the NPE is summed.

For each station the constituent planes are searched for clusters that can be used to form a spacepoint. Spacepoints are constructed from clusters from all three planes (a triplet spacepoint) or from any two out of the three planes (a doublet spacepoint).

6.2.1 Noise

The scintillating fibre trackers operate by registering digits above a given NPE threshold within each fibre plane. Fibres are collected into channels as ganged bundles of 7 for each channel, with digits are registered per channel

instead of per fibre. From a coincidence of digit events in 2 or 3 oblique fibres (fibres in differing planes), a spacepoint is reconstructed, from which track reconstruction can occur. We consider noise in the tracker to be those digits registered not from the passage of a beam particle, but instead from other sources, for instance, dark current from thermal electron emission in the PMTs. To isolate noise from signal during beam-on data collection, a strict cut can be made requiring that only events with one fitted track and 5 spacepoints per tracker are selected, with all 5 spacepoints included in the fitted track. All digits corresponding to the track are then removed from the total set of digits for that event, and the remainder are considered noise digits. An in-situ approximation of active channels for the current data-taking period is made, assuming all channels without at least one registered digit in the selected data-taking run are inactive. The average noise rate per channel per event is then calculated as the total number of event digits above the considered NPE threshold in each tracker, divided by both the active channel number and the number of events satisfying the above selection criteria. This gives a value of 0.18% upstream and 0.06% downstream for events above 2 NPE.

6.2.2 Track Finding Efficiency

Data were analysed in order to determine the track and spacepoint finding efficiency of the detectors during running conditions. A time-of-flight cut was used to ensure that each measured track had a time-of-flight consistent with a muon throughout the entire experimental apparatus. A hit was therefore required in each of the TOF1 and TOF2 detectors, which ensured that the particle must have been successfully transmitted through the cooling channel, crossing both tracking detectors. These requirements ensure that there is a better than 99.9% probability that a particle will have traversed a tracking detector. The number of events missing a track is therefore measured and used to estimate the efficiency of the detector. The results of the efficiency analysis are tabulated in table 2 for a range of momentum and nominal emittances. A track-finding efficiency of 98.70% is reported for the upstream tracker and 98.93% for the downstream tracker, averaged over field and beam conditions. Additionally, assuming a track is found, the probability of successfully finding each spacepoint is summarised in table 3. The overall efficiency of both trackers is sufficient to not present any significant systematic uncertainties in the analysis, however it is lower than the ideal expectation, 99.9% efficiency, due to the presence of dead channels, an unavoidable feature of the construction process.

Momentum	Nominal Emittance	No. Events	Upstream Tracks Found	Downstream Tracks Found
200 MeV/c	6mm	221879	99.42%	96.07%
200 MeV/c	3mm	215229	98.38%	99.19%
140 MeV/c	6mm	180283	98.37%	99.16%
140 MeV/c	10mm	130859	98.47%	98.93%
Averaged		748250	98.70%	98.21%

Table 2: The track finding efficiency for the upstream and downstream trackers for 140 MeV/c and 200 MeV/c beams, and for 3, 6 and 10 mm nominal emittances.

6.2.3 Track Fit Predicted Performance

Monte Carlo simulation used with realistic field and beam conditions in order to estimate the reconstruction performance. Run number 09964 was used (140 MeV/c, 10 mm nominal emittance), representing a typical data set used for the study of emittance evolution. Results are presented in figure 14 for the upstream tracker and figure 15 for the downstream tracker.

Momentum	Nominal Emittance	No. Events	Upstream Spacepoints Found	Downstream Spacepoints Found
200 MeV/c	6mm	221879	99.41%	94.63%
200 MeV/c	3mm	215229	98.04%	97.41%
140 MeV/c	6mm	180283	97.99%	99.16%
140 MeV/c	10mm	130859	98.07%	97.44%
Averaged		748250	98.44%	97.01%

Table 3: The spacepoint finding efficiency, assuming the presence of a track, for the upstream and downstream trackers for 140 MeV/c and 200 MeV/c beams, and for 3, 6 and 10 mm nominal emittances.

6.3 Efficiency evolution

The efficiency of the tracker was processed over the lifetime of its use during the data taking. The analysis used in section 6.2.2 was repeated and automated for runs starting in 2015. The selection included two more constraints: is required a spacepoint to be reconstructed within the tracker volume using a radial cut and that only a single spacepoint is reconstructed in each of the stations, as generally required in most of the analysis.
 325 The evolution of the straight and helical track finding efficiency in the upstream and downstream trackers is shown in figure 16, showing efficiencies generally above 99.0%.

7 Global Track Matching Reconstruction

The overall detector performance can be validated by extrapolating tracks from one detector to another and comparing the reconstructed coordinates with the extrapolated values. Tracks measured in the upstream tracker are extrapolated upstream to TOF1 and TOF0, and downstream to TKD and TOF2. Where there are materials in the beamline, the energy change on passing through the material is estimated using the most probable energy loss. Material thicknesses are approximated by the on-axis thickness.
 330

Particles entering the analysis must satisfy the following criteria:

- 335 • at least one space point must be reconstructed in TOF2;
- one track must be reconstructed in both TKU and TKD. The track in TKD must extrapolate to within the active area of TOF2; and
- the track found in TKD must lie within a radius of 100 mm from the beam axis at the following apertures: the upstream absorber safety window; the upstream absorber window; the absorber centre; the downstream absorber window; the downstream absorber safety window; the upstream edge of SSD; the helium window in SSD; the downstream edge of the downstream PRY aperture.
 340

The final cut restricts the sample to events in which particles are contained within the active area of the experiment and ensures that the selection is consistent across the configurations in which data was taken.

8 Beam-based Detector Alignment

8.1 Introduction

A beam-based alignment algorithm was developed to improve the resolution on the position of the scintillating-fibre trackers lodged inside the bores of superconducting magnets. This method was used to determine the azimuthal orientation of the trackers with a resolution of $6 \text{ mrad}/\sqrt{N}$ and their position with a resolution of $20 \text{ mm}/\sqrt{N}$, where N the number of selected tracks [21].
 345

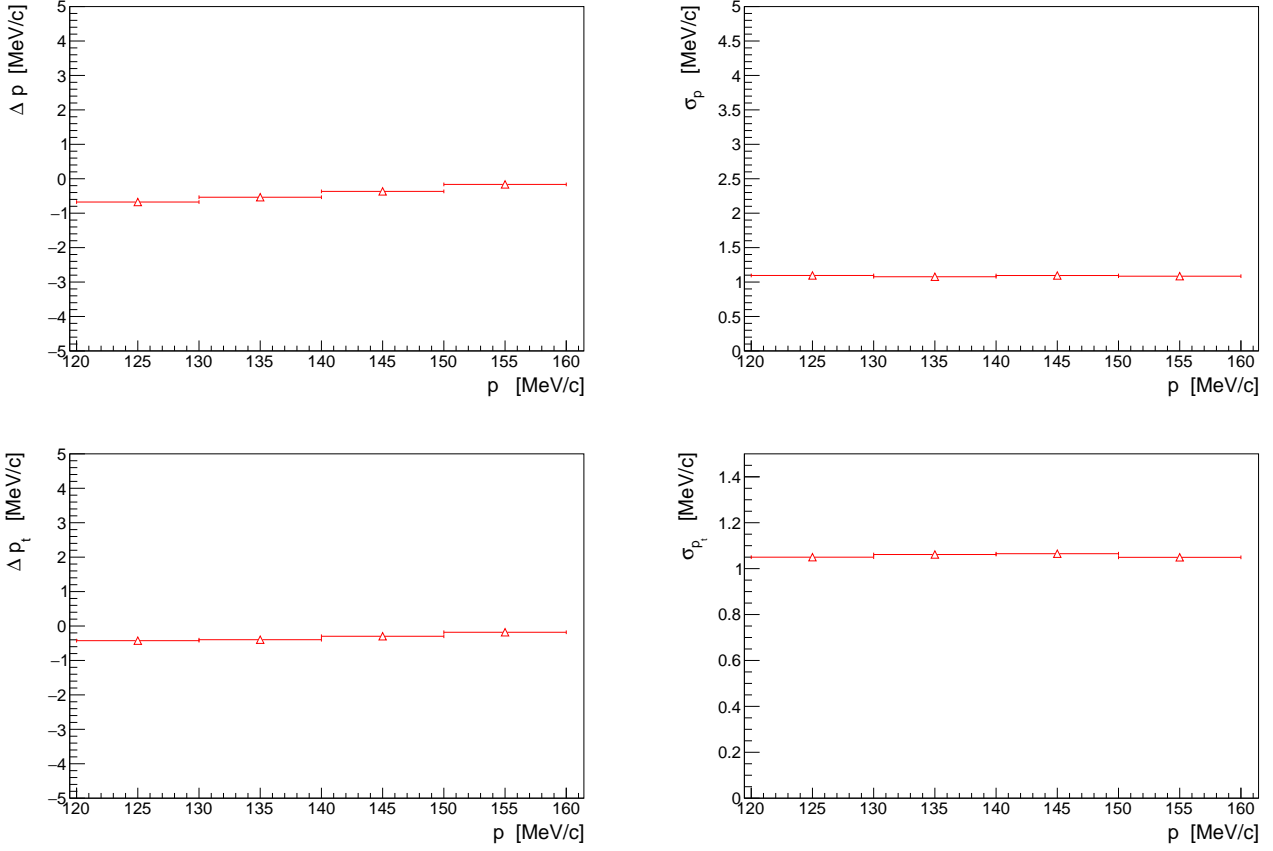


Figure 14: Predicted momentum reconstruction bias (left) and resolution (right) for the longitudinal (top) and transverse (bottom) momentum components in the upstream tracker.

The starting point for the beam-based alignment as the geometrical survey of the detectors in the MICE Hall which was performed using laser telemetry. Only the trackers, nested in the superconducting solenoids, could not be accessed, so their position as inferred with respect to the flanges of the solenoids and the beam-based alignment was used to verify their alignment.

8.2 Analysis method

The position of each tracker in global coordinates is entirely defined by the location of its centre and a set of three angles. Since the position of each tracker along the beamline is known to great accuracy from the survey and the rotation about z has a negligible influence on the alignment, only 4 constants have to be determined for each tracker.

The location of the TOFs is used as the reference for the tracker alignment. The line that joins the centre of TOF1 with the centre of TOF2 is chosen to be the reference axis. A deviation from this axis is considered as a misalignment of the trackers. Multiple scattering in the beam line does not allow formed alignment on single-particle basis. For example, figure 17 shows the path of a single particle that scatters in the absorber module of the MICE experiment. The mean residual angles and positions of the trackers with respect to the TOF12 axis were evaluated to allow the correction factors to be determined.

Each TOF provides a single space point in the global coordinate system. This position is assumed to be the true position with a large uncertainty due to the limited granularity of the detector. Trackers sample the particle track in five different stations and this allows for the reconstruction of a straight track without any assumption

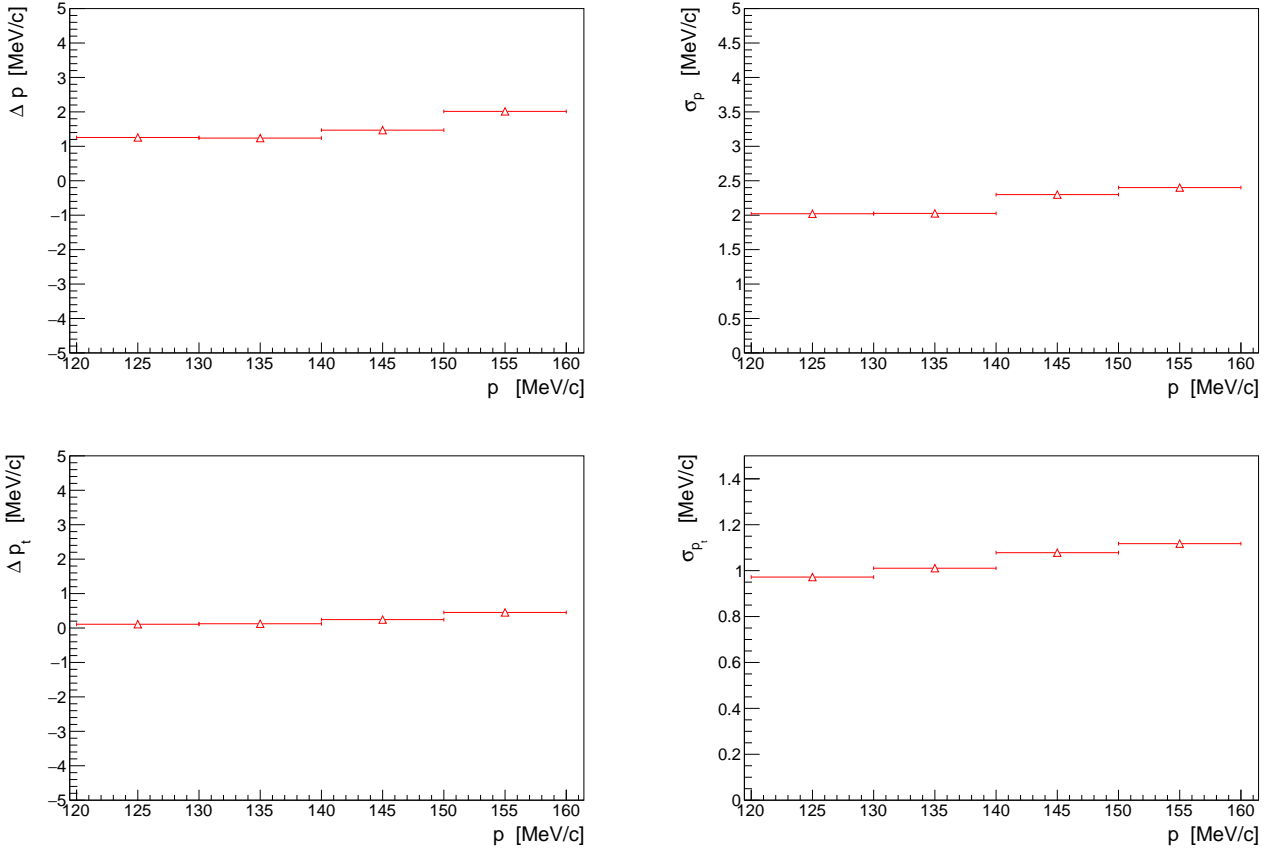


Figure 15: Predicted momentum reconstruction bias (left) and resolution (right) for the longitudinal (top) and transverse (bottom) momentum components in the downstream tracker.

made on the prior position of the tracker. In global coordinates, on average, the track reconstructed between TOF1 and TOF2 should agree with the track reconstructed in either tracker, i.e. the mean residuals should be zero. Applying this reasoning to the unknown offset and angles yields to a system of equations for the four unknown constants [21]. The measurement of four residual distributions per tracker yields the alignment constants. The main source of bias is the scattering in the material between TOF1 and TOF2. If the beam is not perfectly centred, particles preferentially scrape out on one side of the magnet bore, anisotropically truncating the tail of the residual distribution. The selection criteria defined above remove this effect.

Data was recorded with the superconducting magnets of the experiment turned off. High momentum beams were used to reduce the RMS scattering angle and maximise transmission. Each data set was processed independently. Figure 18 shows the alignment parameters measured for each run during a specific ISIS user cycle. The measurements are in good agreement with one another and show no significant discrepancy: an agreement between the independent fits guarantees an unbiased measurement of the alignment constants. The constant fit χ^2/ndf is close to unity for each fit, which indicates that there are no significant additional source of uncertainty. The optimal parameters are summarised in table 4.

	x [mm]	y [mm]	α [mrad]	β [mrad]
TKU	-0.032 ± 0.094	-1.538 ± 0.095	3.382 ± 0.030	0.412 ± 0.029
TKD	-2.958 ± 0.095	2.921 ± 0.096	-0.036 ± 0.030	1.333 ± 0.030

Table 4: Summary table of the optimal alignment constants measured in the high-momentum straight-track data acquired during the 2017/01 ISIS user cycle.

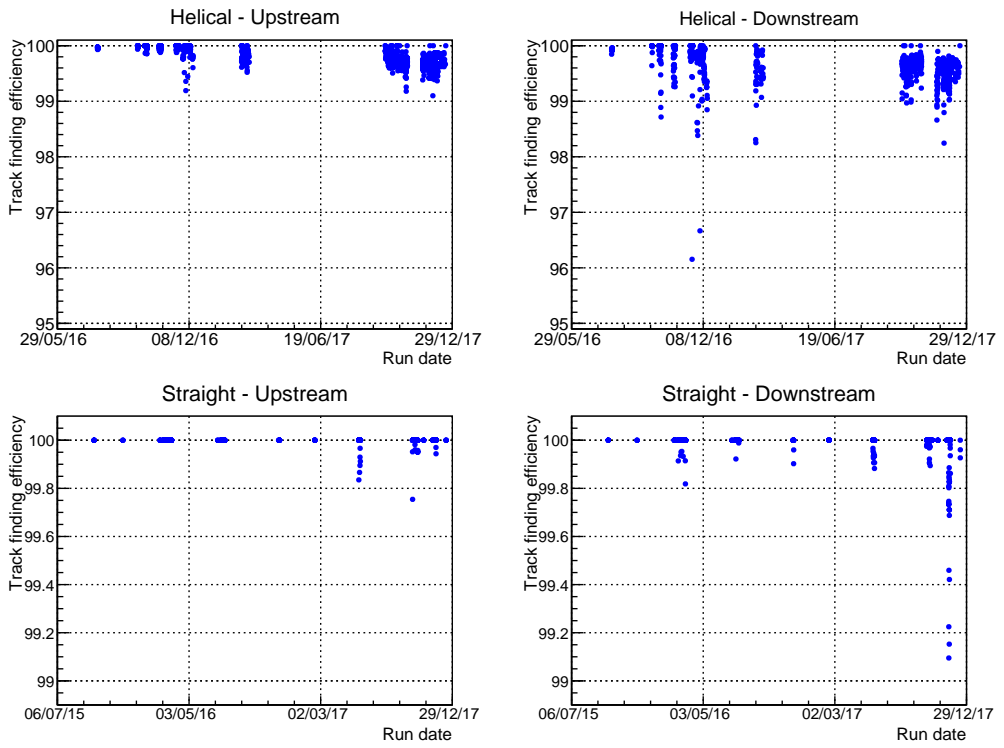


Figure 16: Evolution of the straight and helical track finding efficiency over time for the upstream (left) and downstream (right) trackers during the key periods of data taking since 2015.

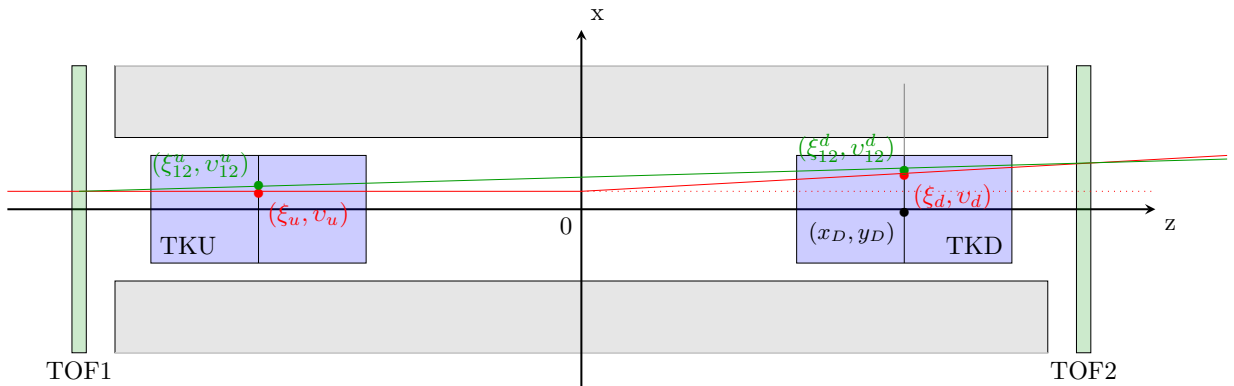


Figure 17: True path of a single particle track (red) and its path as reconstructed from the time-of-flight system (green). The position of the track at the tracker centres is represented by markers.

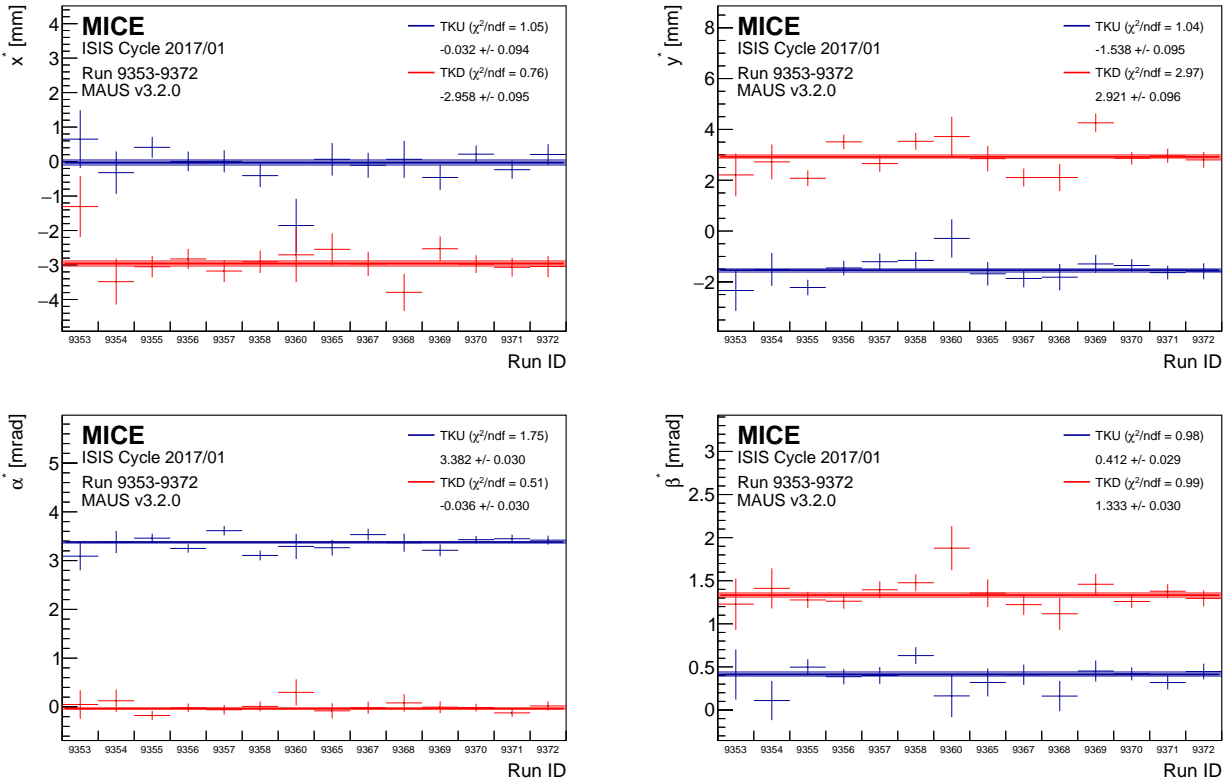


Figure 18: Consistency of the alignment algorithm across runs acquired during the 2017/01 ISIS user cycle.

9 Liquid-Hydrogen Absorber

9.1 Introduction

The absorber vessel comprise a cylindrical aluminium body sealed with two thin aluminium end windows, as shown in figure 19. The absorber vessel was specified to contains 22 l of liquid, so the body had an inner diameter of 300 mm and a length between its end flanges of 230 mm. The length along the central axis between the two domes of the thin aluminium end windows was 350 mm [22].

9.2 Systematic studies

9.2.1 Variation of the density of liquid-hydrogen due to varying temperature and pressure

The energy lost by a muon travelling through the liquid-hydrogen absorber depends on the path length the muon travelled through and on the density of the liquid-hydrogen. The density of liquid-hydrogen is a function of temperature and pressure. The temperature of the vessel was recorded by eight LakeShore Cernox 1050 SD sensors with a resolution of 0.1 K. Four of the sensors were used solely as temperature sensors, while the other four were used also as level sensors to ensure the liquid-hydrogen reached the top of the vessel. They were arranged in pairs with two mechanically clamped at the top of the vessel, two at a rotation of 45°, a further two at a further rotation of 90° and a final two at a further rotation of 45° to be at the bottom of the vessel.

Cooldown and liquefaction were completed slowly over eight days at a pressure of 1.15 Bar after which the

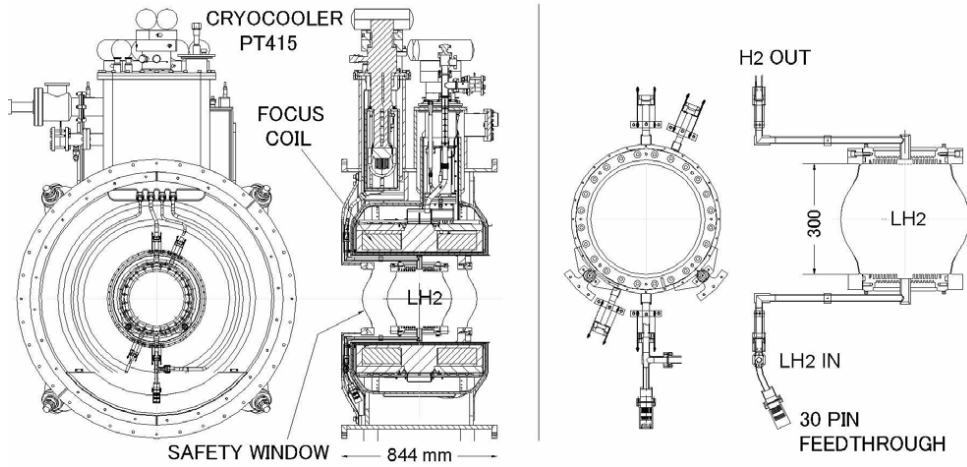


Figure 19: Left panel: Drawing of the absorber/focus-coil (AFC) module showing the principal components. Right panel: detail of the liquid-hydrogen absorber vessel.

vessel's pressure was lowered to 1.085 Bar [22]. The vessel then remained in this steady-state equilibrium until the venting process began. During this process the cryocooler was switched off and the heaters were switched on, delivering a nominal power of 50 Watt to the absorber vessel. This resulted in an increase in pressure and temperature until the temperature stabilised at the boiling point. A rapid increase in temperature was observed once all the liquid-hydrogen had boiled off.

The sensors have a typical accuracy of $\pm 9\text{ mK}$ and a long-term stability of $\pm 12\text{ mK}$ at 20 K. The magnetic-field dependent temperature error at 2.5 T is 0.04%, $\Delta T/T$, equivalent to $\pm 8\text{ mK}$ at 20 K [23][24]. These are the quoted uncertainties given by the manufacturer of the sensors. The importance of magnetic fields on temperature measurements is that they cause reversible calibration shifts: when the magnetic field is removed, the sensors return to their original calibration.

To reduce the uncertainty in the liquid-hydrogen density a calibration procedure was devised using the boiling point: the corrected temperature reading is found by applying a cut-off correction, a magnetic field correction based on the focus coil current and mode, a correction for the non-linearity of the sensors, and a boiling point scaling factor [25].

The boiling point of hydrogen at 1.085 Bar is 20.511 K (figure 20). There are however a number of uncertainties. The sensors have a total uncertainty of 17 mK (9 mK accuracy, 12 mK stability, 8 mK magnetic). The non-linearity of the sensors adds 0.03 K. The temperature scaling and magnet current correction factors also have an associated error as they are based on the 0.1K resolution. For example, a calibrated sensor at boiling temperature and 1.505 Bar should read 21.692 K but can only read 21.65 K (21.6 K cut-off plus 0.05 cut-off correction) i.e. it is off by 0.042 K. The pressure sensors have an uncertainty of $\pm 5\text{ mBar}$ which equates to $\pm 0.016\text{ K}$ during steady state. The pressure uncertainty ($\pm 5\text{ mBar}$) adds another uncertainty to the temperature calibration constants of $\pm 0.014\text{ K}$. Collectively, all these uncertainties add up to 0.2 K for each sensor.

For our steady state condition the liquid-hydrogen was close to the boiling temperature of liquid parahydrogen [25]. The average temperature of the eight sensors during steady-state was $(20.51 \pm 0.07)\text{ K}$ at 1.085 Bar and allows us to determine the uncertainty in the density as $(70.53 \pm 0.08)\text{ kg/m}^3$

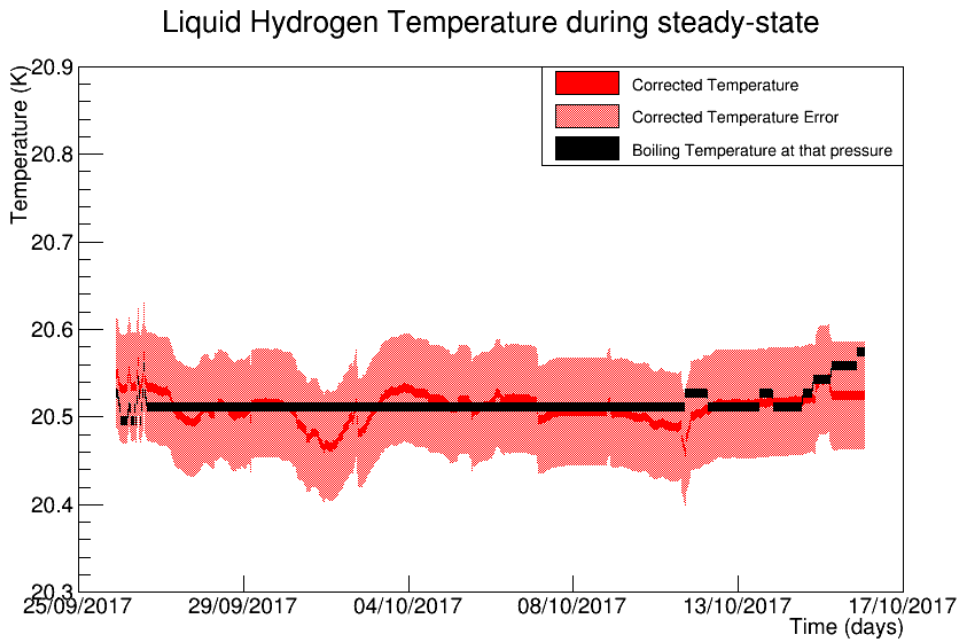


Figure 20: Average LH₂ temperature recorded by the sensors during the steady-state period. After applying all the correction factors the temperature remains at or close to the boiling point temperature.

9.2.2 Contraction of the absorber vessel due to cooling

The aluminium absorber vessel was cooled from room temperature to the operating temperature of the experiment (20.51 K), which resulted in the vessel contracting. The linear contraction of Al-6061 as it is cooled from 293K is given by:

$$\alpha = -4.1277 \times 10^{-3}T - 3.0389 \times 10^{-6}T^2 + 8.7696 \times 10^{-8}T^3 - 9.9821 \times 10^{-11}T^4 \quad (4)$$

where T is the operating temperature [26]. The equation is a line of best fit of data collated by NIST (National Institute of Standards and Technology) and has an associated curve fit error of 4%. At the MICE operating temperature, this corresponds to a linear contraction of the vessel along each plane of 0.415%, resulting in a warm bore length (350 mm) contraction of (1.45 ± 0.05) mm. The vessel was held suspended in place, meaning the vessel was free to contract along each plane without restriction, since the vessel was free to contract within the warm bore of the focus coil.

9.2.3 Deflection of absorber vessel windows due to internal pressure

To minimise energy loss and Coulomb scattering by the absorber vessel, the windows were kept as thin as possible. They must however not rupture when handling any internal pressure they are subjected to. For safety considerations [22][27] it is necessary for the liquid-hydrogen circuit to be pressurised above atmospheric pressure to prevent air ingress. The vessel must also be capable of handling up to 1.5 Bar, the relief valve set pressure.

These pressures resulted in a deflection of the absorber windows and were modelled using ANSYS [28]. The uncertainty in the model's window deflection was 20%. It showed a linear expansion of the window deflection with pressure up to 2 Bar when the windows begin to yield. The pressure sensors are accurate to ± 5 mBar

(0.25% of 2 Bar). At (1085 ± 5) mBar, the typical MICE operating pressure, this corresponds to a deflection of (0.5374 ± 0.1076) mm (model uncertainty) ± 0.0022 mm (sensor uncertainty) at the centre of the absorber window.

⁴⁴⁵ 9.2.4 Variation of the absorber vessel window thicknesses

The amount of energy loss and cooling experienced by a muon passing through the absorber depends on the amount of aluminium and liquid-hydrogen traversed. There are four windows, two absorber wall windows of the vessel and two safety windows.

At the centre of the absorber, the total amount of aluminium the muon beam passes through is (785 ± 13) μm , a variance of 1.68%. However, as the windows were thin, the effects on energy loss are negligible. A $200\text{ MeV}/c$ muon passing along the central axis of an empty absorber loses 0.345 MeV , which introduces a 0.006 MeV uncertainty on energy loss.

9.2.5 Total Systematic Uncertainty on Energy Loss

In total there are three main contributions to the systematic uncertainty of the liquid-hydrogen absorber on energy loss. The contraction of the absorber and deflection of the absorber window due to internal pressure reduces the central warm bore length by (0.4 ± 0.2) mm.

The combined absorber window's thickness variation at the centre of the absorber is $13\text{ }\mu\text{m}$. The average temperature during the steady state period of the experiment when the pressure remained constant at (1085 ± 5) mBar is (20.51 ± 0.07) K corresponding to a liquid-hydrogen density of (70.53 ± 0.08) kg/m³.

⁴⁶⁰ The energy loss is momentum dependent as each particle will lose a different amount of energy passing through the absorber. Tables 5 and 6 show the energy loss at various momenta and densities of Aluminium and liquid-hydrogen [29][30][31][32]. $277\text{ MeV}/c$ and $344\text{ MeV}/c$ are the minimum ionization momenta of Aluminium and liquid-hydrogen respectively.

Table 5: Energy Loss for Aluminium (Al-6061) at various momenta with a density of 2.699 g/cm^3 .

Momentum (MeV/c)	100	140	200	277
Mass Stopping Power ($\text{MeVg}^{-1}\text{cm}^2$)	1.798	1.688	1.630	1.615
Stopping Power (MeVcm^{-1})	4.8528	4.556	4.3994	4.3589

During the MICE experiment muon beam of momentum 140, 170, 200 and $240\text{ MeV}/c$ were used. The ⁴⁶⁵ energy loss and its uncertainty were calculated. The calculation used a central bore length of (349.6 ± 0.2) mm, a total window thickness of (0.785 ± 0.013) mm and a liquid-hydrogen density of (70.53 ± 0.08) kg/m³ for a particle travelling straight through the centre of the absorber.

For a $140\text{ MeV}/c$ muon particle this corresponds to an energy loss of (10.88 ± 0.02) MeV, while for a $200\text{ MeV}/c$ muon particle this corresponds to an energy loss of (10.44 ± 0.02) MeV. In terms of energy loss, the systematic ⁴⁷⁰ error is 0.2%. This is for a particle travelling along the central axis of the absorber. A muon travelling through the absorber in the presence of a magnetic field would take a different path and thus would traverse a different length of aluminium and liquid-hydrogen.

Table 6: Energy loss for liquid-hydrogen at various densities (0.0703 to 0.0708 g/cm³) and various momenta of muons.

Momentum	100	140	200	344
Mass Stopping Power	4.568	4.267	4.104	4.034
Stopping Power (at $\rho=0.0703$)	0.3211	0.29997	0.2885	0.28359
Stopping Power (at $\rho=0.07054$)	0.3222	0.30099	0.2895	0.2846
Stopping Power (at $\rho=0.07078$)	0.3233	0.3020	0.29048	0.2855
Stopping Power (at $\rho=0.0708$)	0.3234	0.3021	0.29056	0.2856

10 Conclusions

A complete set of particle detector have permitted the full characterisation and study of the evolution of the phase space of a muon beam through a section of a cooling channel, leading to the first measurement of ionization cooling with unique level of precision and detail. All the different elements of the MICE instrumentation have been used to characterise the beam and the measurement of the cooling performance for a different variety of beams momenta, emittance, and absorbers. Proving a technique critical for a muon collider and a neutrino factory brings those facilities a step closer.

- [1] S. Geer, “Neutrino beams from muon storage rings: Characteristics and physics potential,” *Physical Review D* **57** no. 11, (Jun, 1998) 6989–6997, arXiv:hep-ph/9712290 [hep-ph].
- [2] D. Neuffer, “Principles and Applications of Muon Cooling,” *Part. Accel.* **14** (1983) 75–90.
- [3] MICE Collaboration, M. Bogomilov *et al.*, “Demonstration of cooling by the Muon Ionization Cooling Experiment,” *Nature* **578** (2020) 53–59, arXiv:1907.08562 [physics.acc-ph].
- [4] M. Bonesini, “The design of MICE TOF0 detector,” *MICE Note 145* (2006) .
<http://mice.iit.edu/micenotes/public/pdf/MICE0145/MICE0145.pdf>.
- [5] R. Bertoni *et al.*, “The construction and laboratory tests for MICE TOF0/1 detectors,” *MICE Note 241* (2008) . <http://mice.iit.edu/micenotes/public/pdf/MICE0241/MICE0241.pdf>.
- [6] R. Bertoni *et al.*, “The design and commissioning of the MICE upstream time-of-flight system,” *Nuclear Instruments and Methods in Physics Research A* **615** (Mar., 2010) 14–26, arXiv:1001.4426 [physics.ins-det].
- [7] R. Bertoni *et al.*, “The construction of the MICE TOF2 detector,” *MICE Note 286* (2010) .
<http://mice.iit.edu/micenotes/public/pdf/MICE0286/MICE0286.pdf>.
- [8] D. Rajaram and V. C. Palladino, “The Status of MICE Step IV,”.
<http://accelconf.web.cern.ch/AccelConf/IPAC2015/papers/thpf122.pdf>.
- [9] M. Bonesini, “Progress of the MICE experiment,” arXiv:1510.08825 [physics.acc-ph].
- [10] The MICE Collaboration, “Characterisation of the muon beams for the Muon Ionisation Cooling Experiment,” *ArXiv e-prints* (June, 2013) , arXiv:1306.1509 [physics.acc-ph].
- [11] D. Adams *et al.*, “Pion contamination in the MICE muon beam,” *Journal of Instrumentation* **11** (Mar., 2016) P03001, arXiv:1511.00556 [physics.ins-det].
- [12] MICE Collaboration, M. Bogomilov *et al.*, “The MICE Muon Beam on ISIS and the beam-line instrumentation of the Muon Ionization Cooling Experiment,” *JINST* **7** (2012) P05009, arXiv:1203.4089 [physics.acc-ph].
- [13] Y. Karadzhov *et al.*, “TOF detectors Time Calibration,” *MICE Note 251* (2009) .
<http://mice.iit.edu/micenotes/public/pdf/MICE0251/MICE0251.pdf>.
- [14] L. Cremaldi *et al.*, “Progress on Cherenkov Reconstruction in MICE,” *MICE Note 473* (2015) .
<http://mice.iit.edu/micenotes/public/pdf/MICE0473/MICE0473.pdf>.
- [15] R. Asfandiyarov *et al.*, “The design and construction of the MICE Electron-Muon Ranger,” *Journal of Instrumentation* **11** (Oct., 2016) T10007, arXiv:1607.04955 [physics.ins-det].
- [16] F. Drielsma, “Electron-Muon Ranger: hardware characterization,” Master’s thesis, University of Geneva, 2014. <https://arxiv.org/abs/1710.06946>.
- [17] D. Adams *et al.*, “Electron-muon ranger: performance in the MICE muon beam,” *Journal of Instrumentation* **10** (Dec., 2015) P12012, arXiv:1510.08306 [physics.ins-det].

- 515 [18] F. Drielsma, *Measurement of the Increase in Phase Space Density of a Muon Beam through Ionization Cooling*. PhD thesis, University of Geneva, 10, 2018.
- [19] M. Ellis *et al.*, “The Design, construction and performance of the MICE scintillating fibre trackers,” *Nucl. Instrum. Meth.* **A659** (2011) 136–153, 1005.3491.
- 520 [20] **D0** Collaboration, V. M. Abazov *et al.*, “The Upgraded D0 detector,” *Nucl. Instrum. Meth.* **A565** (2006) 463–537, physics/0507191.
- [21] F. Drielsma, “Beam-based detector alignment in the MICE muon beam line,” arXiv:1805.06623 [physics.ins-det]. <https://arxiv.org/abs/1805.06623>.
- [22] V. Bayliss *et al.*, “The liquid-hydrogen absorber for mice,” *Journal of Instrumentation* **13** no. 09, (2018) T09008. <http://stacks.iop.org/1748-0221/13/i=09/a=T09008>.
- 525 [23] “Cernox RTDs [Accessed 2 Oct. 2018],”.
https://www.lakeshore.com/Documents/LSTC_Cernox_1.pdf.
- [24] “Temperature Measurement and Control Catalog [Accessed 2 Oct. 2018],”.
https://www.lakeshore.com/Documents/LakeShoreTC_1.pdf.
- 530 [25] C. Brown *et al.*, “Systematic Uncertainties in the LH2 absorber,” *MICE Note 524* (2018).
<http://mice.iit.edu/micenotes/public/pdf/MICE0524/MICE0524.pdf>.
- [26] G. Hardin, “Aluminum 6061-T6 (UNS AA96061) [Accessed 3 Oct. 2018],”.
<https://www.nist.gov/mml/acmd/aluminum-6061-t6-uns-aa96061>.
- [27] S. Ishimoto *et al.*, “Liquid Hydrogen Absorber for MICE,” *Conf. Proc. C100523* (2010) 421–423.
- 535 [28] M. Green *et al.*, “Does One Know the Properties of a MICE Solid or Liquid Absorber to Better than 0.3 Percent?,” *MICE Note 155* (2006).
<http://mice.iit.edu/micenotes/public/pdf/MICE0155/MICE0155.pdf>.
- [29] “Atomic and nuclear properties of Aluminium,”.
http://pdg.lbl.gov/2017/AtomicNuclearProperties/HTML/aluminum_Al.html.
- 540 [30] “Atomic and nuclear properties of liquid Hydrogen,”. http://pdg.lbl.gov/2017/AtomicNuclearProperties/HTML/liquid_hydrogen.html.
- [31] “Muon in Aluminium,”. http://pdg.lbl.gov/2017/AtomicNuclearProperties/MUE/muE_aluminum_Al.pdf.
- [32] “Muons in liquid Hydrogen,”. http://pdg.lbl.gov/2017/AtomicNuclearProperties/MUE/muE_liquid_hydrogen.pdf.